NEOPLASIA
www.neoplasia.com

Volume 19 Number 4 April 2017 pp. 310–320 310

Noninvasive Bioluminescence Imaging of AKT Kinase Activity in Subcutaneous and Orthotopic NSCLC Xenografts: Correlation of AKT Activity with Tumor Growth Kinetics[1]

Karina Suchowski*, Thomas Pöschinger*, Alnawaz Rehemtulla†, Michael Stürzl‡ and Werner Scheuer*

*Discovery Oncology, Pharmaceutical Research and Early Development (pRED), Roche Innovation Center Munich, Penzberg, Germany; †Department of Radiation Oncology, University of Michigan Medical School, Ann Arbor, MI, USA; ‡Division of Molecular and Experimental Surgery, Department of Surgery, University Medical Center Erlangen, Friedrich-Alexander University of Erlangen-Nuremberg, Erlangen, Germany

Abstract

Aberrant signaling through the AKT kinase mediates oncogenic phenotypes including cell proliferation, survival, and therapeutic resistance. Here, we utilize a bioluminescence reporter for AKT kinase activity (BAR) to noninvasively assess the therapeutic efficacy of the EGFR inhibitor erlotinib in KRAS-mutated lung cancer therapy. A549 non–small cell lung cancer cell line, engineered to express BAR, enabled the evaluation of compounds targeting the EGFR/PI3K/AKT pathway *in vitro* as well as in mouse models. We found that erlotinib treatment of resistant A549 subcutaneous and orthotopic xenografts resulted in significant AKT inhibition as determined by an 8- to 13-fold ($P < .0001$) increase in reporter activity 3 hours after erlotinib (100 mg/kg) administration compared to the control. This was confirmed by a 25% ($P < .0001$) decrease in pAKT *ex vivo* and a decrease in tumor growth. Treatment of the orthotopic xenograft with varying doses of erlotinib (25, 50, and 100 mg/kg) revealed a dose- and time-dependent increase in reporter activity (10-, 12-, and 23-fold). Correspondingly, a decrease in phospho-AKT levels (0%, 16%, and 28%, respectively) and a decrease in the AKT dependent proliferation marker PCNA (0%, 50%, and 50%) were observed. We applied μ-CT imaging for noninvasive longitudinal quantification of lung tumor load which revealed a corresponding decrease in tumor growth in a dose-dependent manner. These findings demonstrate the utility of BAR to noninvasively monitor AKT activity in preclinical studies in response to AKT modulating agents. These results also demonstrate that BAR can be applied to study drug dosing, drug combinations, and treatment efficacy in orthotopic mouse lung tumor models.

Neoplasia (2017) 19, 310–320

Introduction

Lung cancer is the most lethal malignancy for both men and women in the United States with an estimated death rate of 27%. Non–small cell lung cancer (NSCLC), the most common subtype, suffers from a 5-year survival of about 15% [1,2]. Surgery followed by cytotoxic chemotherapy or radiation remains standard care in early disease. Nevertheless, 70% of the patients are diagnosed with advanced disease where more effective therapies are needed to improve outcomes [1]. Oncogenic mutations such as EGFR, KRAS, HER2, EML4-ALK, and MET have been investigated as targets for personalized therapy [3–5]. For example, targeting EGFR using erlotinib (Tarceva) or gefitinib (Iressa) constitutes a promising therapeutic approach for the 10% to 30% of NSCLC patients harboring activating mutations but a modest benefit for patients with wild-type EGFR [6]. Following an initial response, the vast majority

Address all correspondence to: Karina Suchowski, MSc, Pharma Research & Early Development (pRED), Roche Diagnostics GmbH, Nonnenwald 2, Penzberg, Germany. E-mail: Karina.Suchowski@roche.com

[1] Funding: This research did not receive any specific grant from funding agencies in the public, commercial, or not-for-profit sectors.
Received 5 October 2016; Revised 31 January 2017; Accepted 6 February 2017

© 2017 The Authors. Published by Elsevier Inc. on behalf of Neoplasia Press, Inc. This is an open access article under the CC BY-NC-ND license (http://creativecommons.org/licenses/by-nc-nd/4.0/).

1476-5586
http://dx.doi.org/10.1016/j.neo.2017.02.005

of patients develop resistance to therapy which results in disease progression. Numerous molecular mechanisms have been identified to drive resistance to EGFR tyrosine kinase inhibitors (TKIs) [6–8]. Constitutively activated AKT signaling has been found to be associated with acquired resistance to EGFR-TKIs in NSCLC [9] as well as chemotherapy or radiotherapy [10,11].

In healthy tissue, the serine/threonine kinase AKT functions as a central node for intracellular signaling pathways that regulate cell proliferation, survival, glucose metabolism, and angiogenesis [12]. In response to extracellular growth factor stimulation, PI3-kinase is activated to phosphorylate phosphatidylinositol-3, 4-bisphosphate (PIP2), generating phosphatidylinsitol-3, 4, 5-triphosphate (PIP3). PIP3 recruits AKT to the plasma membrane where AKT is activated in a phosphorylation-dependent manner. Once activated, AKT can phosphorylate downstream signaling cascades including nuclear factor κB (NF-κB) [13], proline-rich AKT substrate of 40 kDa (PRAS40), and tuberous sclerosis complex 2 (TSC2) [14], as well as forkhead box O (FoxO) family proteins [15]. Further prominent downstream effectors include the Bcl-2-family members Bad, Bax, Bim, and glycogen synthase kinase-3 (GSK-3) [16–18] (Figure 1). Deregulated activation of AKT is a hallmark of many human cancers [19]. Research over the past decades has revealed hyperactivation of PI3K/AKT for many human malignancies including NSCLC [20,21]. AKT is intensively studied as a target, and AKT inhibitors are considered attractive as a combination therapy to overcome resistance [22,23]. For the development of successful preclinical EGFR/PI3K/AKT pathway inhibiting therapies, the ability to monitor AKT activation status *in vivo* in real time and in a noninvasive manner would be of great benefit to define optimal combination strategies for subsequent clinical trials.

Optical imaging (bioluminescence and fluorescence) has been utilized at various stages in the drug development process to facilitate rapid monitoring of intracellular events in a noninvasive and dynamic manner [24,25]. We previously reported on the application of a bioluminescent reporter for apoptosis using protein complementation technology [26]. In this study, we evaluated AKT specific kinase activity using the bioluminescent AKT reporter (BAR), which has been described previously [27]. In the presence of AKT kinase activity, luciferase activity of the reporter is minimal due to phosphorylation-dependent steric constrains within the reporter.

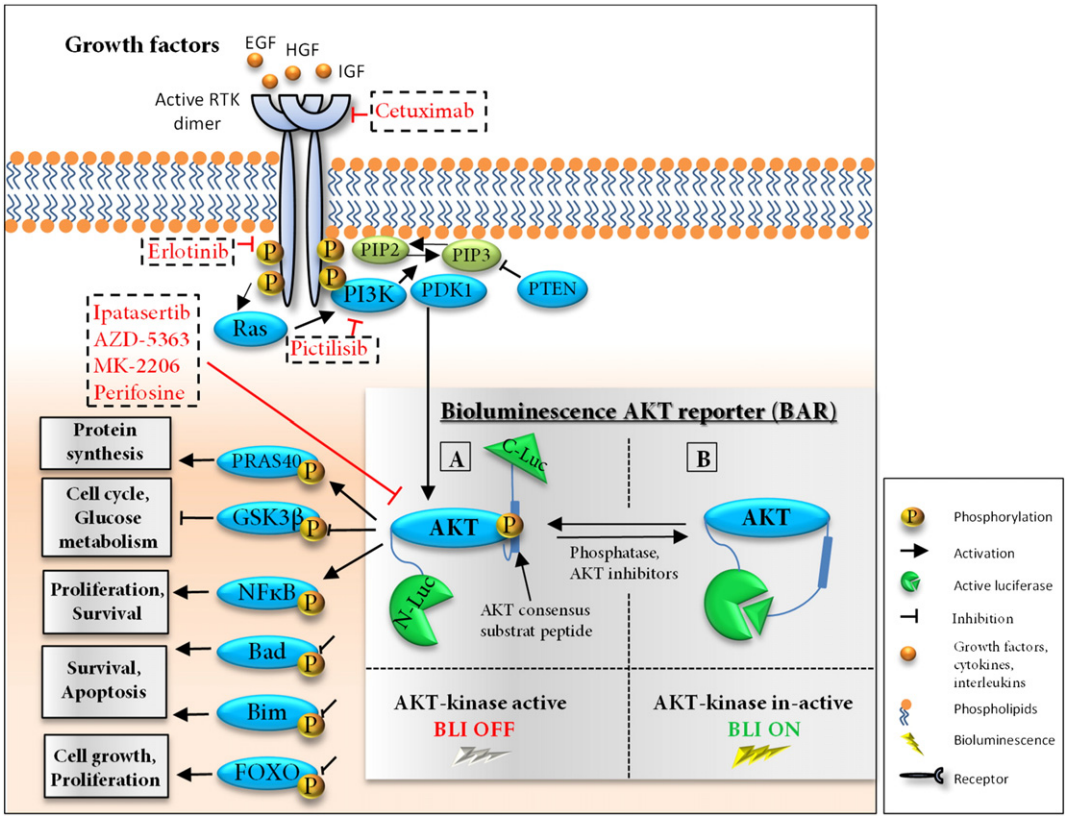

Figure 1. Principle of the bioluminescence AKT reporter (BAR). EGFR/PI3K signaling cascade phosphorylates the serine/threonine kinase AKT, responsible for several tumor-associated cell processes such as cell growth, proliferation, protein synthesis, and aberrant glucose metabolism. The blockage of AKT induces apoptosis and growth inhibition. (A) The reporter contains the N-terminal (N-luc) and C-terminal (C-luc) domains of the firefly luciferase and the AKT consensus substrate peptide [27]. Phosphorylation of the reporter construct by AKT sterically inhibits complementation of the firefly luciferase domains (kinase active; BLI signal off). (B) Dephosphorylation permits luciferase complementation (kinase inactive; BLI signal on) [27]. RTK, Receptor tyrosine kinase; PI3K, phosphatidylinositol 3-kinase; Ras; rat sarcoma; PIP2, phosphatidylinositol4,5-bisphosphate, PIP3, phosphatidylinositol 3,4,5-trisphosphate; PTEN, phosphatase and tensin homolog; PDK1, 3-phosphoinositide dependent protein kinase-1; AKT, protein kinase B; GSK3β, glycogen synthase kinase 3 beta; PRAS40, proline-rich AKT substrate of 40 kDa; NFkB, nuclear Factor kappaB; Bim, B-cell lymphoma 2 interacting mediator of cell death; Bad, Bcl-2-associated death promoter; FOXO, forkhead-box-proteins; EGF, epidermal growth factor; HGF, hepatocyte growth factor; IGF, insulin growth factor.

The inhibition of the AKT kinase activity (i.e., in response to an inhibitor) decreases the phosphorylation of the reporter and releases the steric constrain which results in protein complementation and an increase in bioluminescence activity (Figure 1). BAR therefore provides stable, robust, and reproducible pharmacodynamic readout for high-throughput analysis of AKT targeted agents *in vitro* and *in vivo*. In this study, we also included μ-CT (commonly applied for lung imaging) as independent validation of findings derived using BAR to assess the therapeutic efficacy of erlotinib.

Materials and Methods

Chemicals and Reagents

The EGFR inhibitor erlontib (Roche GmbH, Mannheim, Germany) was used for *in vitro* and *in vivo* studies. For *in vivo* application, it was formulated into sterile 3% Captisol (Ligand Pharmaceuticals, San Diego, CA) and stored at 4°C. In addition, Perifosine, Ipatasertib (GDC-0068), Pictilisib (GDC-0941), MK-2206, AMG-5363 (from Selleck Chemicals, Houston, TX), and Cetuximab (Erbitux, Merck chemicals GmbH, Darmstadt, Germany) were tested *in vitro.* D-luciferin firefly potassium salt (Promega GmbH, Madison, WI) was dissolved into sterile DPBS (PAN Biotech GmbH, Aidenbach, Germany) and stored during the study at −20°C.

Cell Line and Culture

The NSCLC cell line A549, stably transfected by the split-luciferase bioluminescence AKT reporter construct (short BAR), developed by the Center for Molecular Imaging, Ann Arbor, MI [27], was used and cultured in RPMI 1640 medium supplemented with 10% FCS, 2 mM glutamine (both PAN Biotech GmbH, Aidenbach, Germany), and 10 μg/ml Blasticidin (InvivoGen, San Diego, CA. The cell line was tested negative for pathogens by molecular diagnostics infectious disease PCR (Charles River, Wilmington, MA) and maintained at 37°C, 5% CO_2 in a humidified incubator.

Bioluminescence Assay In Vitro

To achieve live-cell bioluminescence imaging, A549-BAR cells (15,000 cells/well; 100 μl per well) were seeded into white, clear-bottom 96-well microplates (PerkinElmer, Groningen, Netherlands) and incubated overnight. Afterwards, cells were treated with various inhibitors for 1 hour at 37°C; D-luciferin was added at a final concentration of 120 μg/ml. The photon counts for each condition (n = 6) were measured 5 minutes after luciferin addition by the Safire2 plate reader (Tecan Group Ltd., Männedorf, Switzerland). The mean bioluminescence induction of the reporter signal was divided by the mean of untreated cells at the distinct time points to get fold induction.

Western Blot Analysis

A549-BAR cells (1×10^6 cells per six-well plate; 2 ml per well) were treated with various inhibitors or left untreated at time points indicated in the figure legend. Cells were lysed at 4°C according to the manufacturer's instructions (Bio-PlexTM cell lysis kit, Bio-Rad Laboratories, Hercules, CA). The lysate protein concentration was determined by Pierce BCA assay (Thermo Fisher Scientific Waltham, MA). The protein extract (5 μg) was mixed with NuPAGE LDS Sample Buffer and NuPAGE sample reducing agent heated at 75°C for 10 minutes and separated by NuPAGE 4% to 12% gradient sodium dodecyl sulfate gel. Proteins were transferred onto a nitrocellulose membrane using the Novex semi-dry-blotter (all Invitrogen, Carlsbad, CA). Blots were blocked for 1 hour in TBST buffer (TBS-0.1% Tween-20) containing 5% nonfat dried milk at RT (from Carl Roth GmbH, Karlsruhe, Germany). Afterward, blots were incubated with 1 μg/ml of antibodies against pAKT1 (Ser473), AKT1, pEGFR (Y1068), EGFR, pGSK3β (Ser9), GSK3β, pRAS40 (Thr246), RAS40 (all 1 hour; 1:1000), and anti–β-actin HRP-linked antibody (1 hour; 1:2000) (all from Cell Signaling, Bad Homburg, Germany). After washing in TBST, blots were incubated (1 hour; 1:2000) with the secondary anti-rabbit IgG HRP-linked antibody (Cell Signaling Technology, Danvers, MA). The SuperSignal West Femto Substrate Mix (Thermo Fisher Scientific Waltham, MA) was added followed by detection with the chemoluminescence system (GE Healthcare Life Sciences, Freiburg, Germany). Recombinant protein standards (Invitrogen, Karlsruhe, Germany) were used for molecular mass determination. For antibody dilution, TBST buffer with 5% nonfat dried milk was used. Protein levels were analyzed by NIH ImageJ software and normalized to β-actin, and results are represented in arbitrary units.

Animals and Xenograft Models

Severe combined immunodeficient (Scid) beige mice (weight from 20 to 27 g) were obtained from Charles River Laboratories (Sulzfeld, Germany). All animals (age of 7-9 weeks) were maintained in the animal facility of Roche GmbH Penzberg (AAALAC certified) under specific pathogen-free conditions with natural daylight cycles (12-hour light/12-hour dark) at 22°C, 55% humidity. All experiments were conducted in accordance with the German Animal Welfare Act (http://www.gesetze-im-internet.de/tierschg/ BJNR012770972.html) and were reviewed and approved by the local governmental animal ethics committee.

To establish subcutaneous (s.c.) A549 xenografts, mice were anesthetized (under 2% isoflurane), and 100-μl cell suspension (5×10^7 cells/ml suspended in DPBS) was inoculated in the right flank of each mouse. Tumor volumes [(length × width^2)/2] were measured by caliper twice weekly. When the tumors reached 60 to 100 mm^3, mice were randomized and treatment was initiated. Erlotinib 100 mg/kg or vehicle control was applied daily per os for 7 days (n = 8). The change of the tumor cell growth was calculated by the mean end point tumor volumes of each group divided by initial mean tumor volumes. The tumor growth inhibition was calculated according to the formula $(1-[(T-T0)/(C-C0)]) \times 100$ (T: tumor volume in the treated group at measurement; T0: tumor volume in the treated group at baseline; C: tumor volume in the control group at measurement; C0: tumor volume in the control group at baseline).

To establish orthotopic xenografts, $5x10^6$ cells in 100 μl were injected into the tail vein of the mouse. Tumor growth was monitored by weekly measurement of bioluminescence signal intensities localized in the lungs of mice. Based on the basal reporter BLI-activity, mice were selected into the treatment groups. The treatment was started 22 or 25 days after inoculation of tumor cells. For short time treatment three different doses of erlotinib (25 mg/kg, 50 mg/kg, and 100 mg/kg) as well as vehicle control were applied daily per os twice (n = 4). For long-time treatment, erlotinib was administered daily for 2 weeks in two concentrations (25 or 100 mg/kg; q5d × 2w; n = 8).

The lung tumor growth was monitored noninvasively using μ-CT imaging. Three percent Captisol solution was used as the vehicle control for both the s.c. and orthotopic model.

Bioluminescence Imaging In Vivo

Mice were injected i.p. with 100 μl of D-luciferin (150 mg/kg; Promega GmbH, Madison, WI) and anesthetized with 2% isoflurane during imaging. Bioluminescence measurement was acquired 10 minutes after luciferin application with an IVIS Spectrum (Caliper Life Sciences, Hopkinton, USA). The signal analysis was performed with Living Image software (Caliper Life Sciences, Hopkinton, USA). The circular region of interest (ROI) over the tumor or lung was measured as average radiance [p/s/cm^3/sr]. Each single ROI signal was divided by the ROI signal measured before the treatment to calculate the fold induction of each individual mouse. BLI signals were always expressed as fold induction.

In Vivo Micro-CT Imaging

Micro-CT (μ-CT) imaging at pre- and posttreatment periods allows longitudinal follow-up of an individual animal. All mice were scanned in a preclinical dual-source micro-CT scanner (TomoScope Synergy Twin, CT Imaging GmbH, Erlangen, Germany). This cone-beam scanner is equipped with a high-speed flat-panel detector with CsI-scintillator which allows to image an object of 65-mm diameter with a spatial resolution of ~80 μm. Mice were anesthetized with 2% isoflurane (at 2 l/min oxygen), placed on the mouse tray, and scanned using 50 kV and 0.8 mA. The μ-CT image acquisition resulted in 1440 projections collected in a full 360° rotation of the gantry during 180 seconds. Mice of the orthotopic A549-BAR xenograft model were imaged at day 26, 32, and 36 after cell inoculation, whereby the treatment was initiated at day 26. The data set was reconstructed based on a Feldkamp-type reconstruction algorithm (CT Imaging GmbH), with a voxel size of 35 μm^3 (35 × 35 × 35 μm).

Micro-CT Data Analysis

The reconstructed data sets were viewed and analyzed using open-source DICOM viewer software (OsiriX). First, μ-CT data were inverted and cropped to display the mouse lung. The lung-air volume (LAV) segmentation was performed semiautomated allying a threshold of (–) 350 to (–) 800 HU.

Tissue Preparation and Immunohistochemistry

Mice were sacrificed 3 to 4 hours after the last erlotinib application by cervical dislocation. For immunohistochemical (IHC) analyses, paraffin-embedded tissue of mouse tumor or lung was sectioned (1.5 μm) using a rotary microtome (Leica, London, UK), floated onto water (42°C), collected on SuperfrostPlus slides (VWR, UK), and dried overnight (incubator, 37°C). Afterwards, they were deparaffinized through xylene and a graded series of ethanol solutions. The antigen retrieval was performed by heating the slides in citrate buffer (pH 6) at 96°C for 10 minutes. Nonspecific binding was blocked by incubation with blocking buffer (Dako GmbH, Hamburg, Germany) for 1 hour at room temperature. The slices were incubated with primary antibodies diluted in blocking buffer. Anti-pAKT (Ser473; 1 hour; 1:50), proliferating cell nuclear antigen (PCNA) (1 hour; 1:50) (from Abcam, Cambridge, MA), and anti-cleaved Caspase-3 (1:300, overnight, Cell Signaling, Danvers, MA) were incubated. Rabbit monoclonal antibody served as a negative control. Subsequently, slides were washed into TBST, and detection of the primary antibodies was assessed by incubation of anti-rabbit IgG Alexa Fluor-488 F(ab)$_2$ (1:200, 1 hour; Invitrogen, Darmstadt, Germany). The tissue sections were washed and coverslipped with Fluoro-Gel II with DAPI (Electron Microscopy Sciences, Hatfield, PA). Imaging and analysis were done by multispectral fluorescence microscopy using Pannoramic 250 1.14 slide scanner and Pannoramic Viewer 1.15 (3DHistech, Budapest, Hungary) at fluorescence excitation and emission maxima for Alexa Flour dye and DAPI. Analysis of staining was performed with in-house–developed FluoImageThreshTool software (Roche GmbH, pRED Informatics, Penzberg).

Statistical Analysis

All data values are represented as mean ± standard error of the mean (SEM). Statistical analysis was performed using GraphPad Prism 6 software (GraphPad Software, La Jolla, CA). Two-sided pairwise *t* test was applied for *in vitro* and *in vivo* analysis. P values < .05 were considered as statistically significant.

Results

Correlation of BAR Activity with Phospho-AKT Levels in A549 Lung Cancer Cells In Vitro

First, the functionality of the bioluminescence AKT reporter (BAR) for subsequent *in vivo* therapy studies was validated *in vitro*. A549-BAR cells were treated with various compounds for 1 hour to evaluate their ability to induce a bioluminescence signal (Figure 2*A*). Treatment with erlotinib (EGFR inhibitor), pictilisib (PI3K inhibitor), MK-2206, as well as perifosine (both AKT inhibitors) resulted in a 2.5- to 5-fold increase in bioluminescence activity in a concentration-dependent fashion. The exposure of the cells to cetuximab (EGFR inhibitor), ipatasertib, and AZD-5363 (both ATP-competitive AKT inhibitors) only resulted in a marginal change of the BLI-activity (1- to 1.5-fold). To confirm these data, the phosphorylation status of AKT (Ser473) and of its substrates PRAS40 (proline rich AKT substrate) and GSK3β (glycogen synthetase kinase-3 beta) was evaluated by Western blot analysis (Figure 2*B*). We detected a corresponding decrease of pAKT, pPRAS40, and pGSK3β in whole-cell lysates when the BAR activity was maximal. The ATP-competitive inhibitors ipatasertib and AZD-5363 inhibited the phosphorylation of RAS40 and GSK3β despite an intense pAKT Western blot band. Additionally, protein analysis confirmed a decrease in AKT activation as a result of blocking EGFR by erlotinib (as well as a decrease in pGSK3β; whereas pRAS40 remained high). When A549-BAR cells were treated with cetuximab, BAR-activity and pAKT levels remained unchanged (Figure 2, *A* and *B*). Finally, peak BLI-signal correlated with the phosphorylation status of AKT (Figure 2*C*). The results demonstrate that BAR activity can be used as a noninvasive surrogate for AKT kinase activity in cells.

In Vivo Imaging of BAR Activity in Subcutaneous A549 Lung Cancer Xenografts Correlates with AKT Activation Status and Therapeutic Tumor Response

After *in vitro* validation, we evaluated the BAR in s.c. A549 xenografts *in vivo.* The tumor growth was monitored by caliper measurements. Tumor-bearing mice treated with 100 mg/kg erlotinib daily demonstrated an 8- to 13-fold induction of bioluminescence activity after each treatment cycle (Figure 3, *A* and *B*). The BLI signals for untreated mice remained unchanged. The BLI signal intensities were recorded at indicated time points after erlotinib application at 5 treatment days. To confirm that the *in vivo* changes in BAR activity resulted from inhibition of AKT kinase activity, IHC analysis of the tumors was performed. Staining of tumor sections with anti-pAKT specific antibody showed a decrease in pAKT levels (25%) after seven treatments with 100 mg/kg erlotinib compared to the untreated animals (Figure 3, *C* and *D*). In addition,

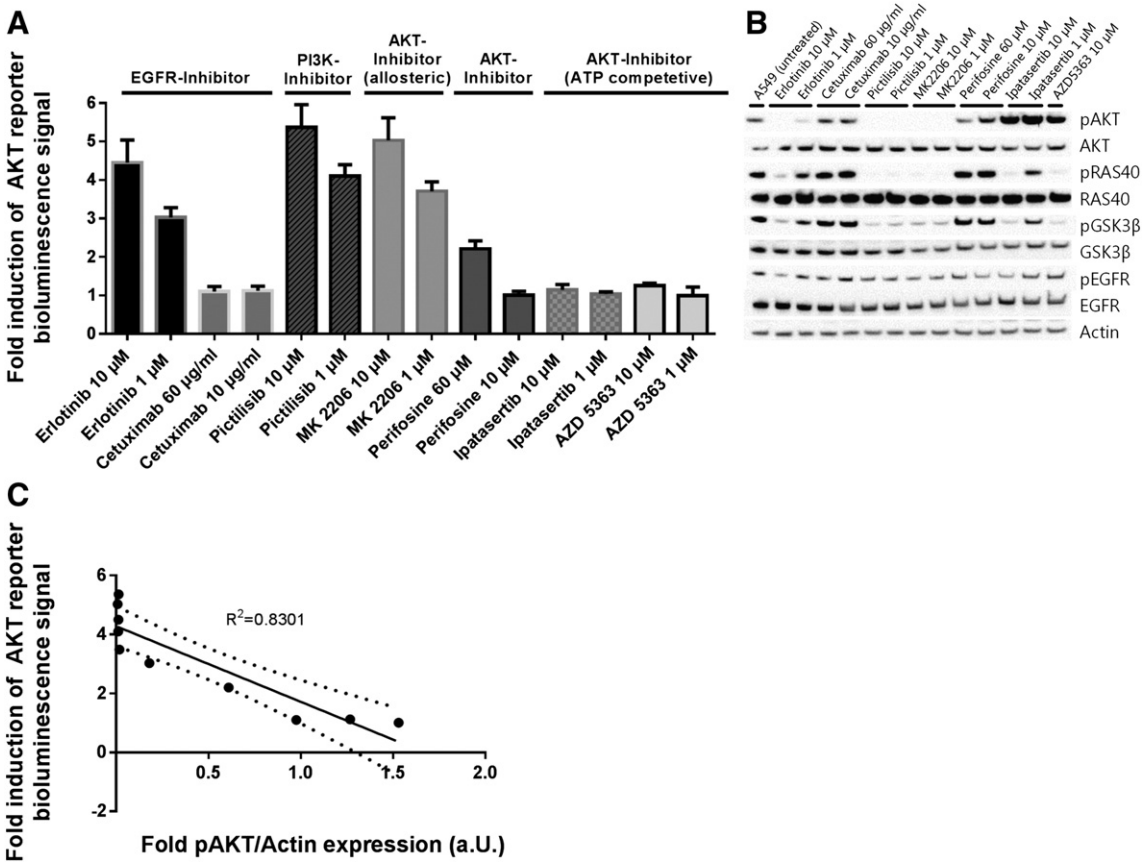

Figure 2. *In vitro* evaluation of BAR activity in A549-BAR cell line. (A) Bioluminescence activity was quantified 1 hour after treatment in response to various compounds at two concentrations ($n = 6$). (B) Western blotting analysis after 1 hour of treatment showing the expression of pAKT (Ser473), AKT, pPRAS40 (Thr246), RAS40, pGSK3β (Ser9), GSK3β, pEGFR (Tyr1068), EGFR, and β-Actin of whole cell lysates. (C) The correlation graph displaying the BAR activity with pAKT status quantified in arbitrary units by analyzing bands on a Western blot.

erlotinib treatment also resulted in a significant tumor growth inhibition of 36% after 7 days (Figure 3*E*; $P < .01$). This indicates that activation of BAR activity correlated with a decrease in pAKT levels and translated into tumor growth reduction in s.c. xenografts.

In Vivo Imaging of AKT Kinase Activity in Orthotopic Lung Cancer Xenografts Reveals Peak Inhibition between 2.5 Hours and 3 Hours after Erlotinib Treatment

After demonstrating that BAR activity correlated with AKT activation status *in vivo* using an s.c. xenograft model, we evaluated the reporter in an orthotopic A549 lung cancer model. Mice bearing orthotopic tumors were treated with various doses of erlotinib (25, 50, and 100 mg/kg; Figure 4, *A* and *B*). Mice treated with the highest dose of erlotinib (100 mg/kg) showed a 10-fold induction in bioluminescence within 2.5 hours after treatment, which remained high over 6 hours (Figure 4*B*). At lower dosages, 50 mg/kg as well as 25 mg/kg, the reporter BLI signal increased four- to six-fold (2.5 hours), but signal intensities declined rapidly within 4 hours ($P < .05$; Figure 4*B*). No significant change in BLI activity was detected in the vehicle group. Erlotinib readministration 24 hours later instantly resulted in an inhibition of AKT activity measured 2.5 hours after administration comparable to the first treatment. A third BLI measurement performed only 30 minutes later revealed a prominent inhibition of the phosphorylation status for all dosages tested (BAR activity was 10-fold, 12-fold, and 23-fold after treatment with 25, 50, and 100 mg/kg erlotinib, respectively). Subsequently, the BLI signal decreased in a comparable fashion to the first drug application (not shown). These results using the BAR reporter reveal that peak inhibition occurred between 2.5 and 3 hours after drug application (Figure 4, *A* and *B*).

To confirm that the dose-dependent increase in reporter activity resulted from AKT inhibition, we performed *ex vivo* IHC analysis using a pAKT specific antibody of the lung sections. The staining of the sections showed a decrease in the pAKT levels (28%) after two treatments with 100 mg/kg erlotinib. In mice treated with 50 mg/kg erlotinib, a 16% reduction in pAKT expression was observed (Figure 4, *C* and *D*). Additionally, the AKT-dependent cell proliferation marker PCNA was assessed (Figure 4, *E* and *F*). The amount of PCNA-positive cells decreased by 50% after two treatments with erlotinib at 50 and 100 mg/kg ($P < .001$). In contrast, 25-mg/kg erlotinib application altered neither AKT phosphorylation levels nor PCNA expression significantly compared to the vehicle group (Figure 4, *C*–*F*). The observed induction of BAR-activity by erlotinib *in vivo* was consistent with the observed changes in pAKT levels and the AKT-dependent proliferation marker PCNA *ex vivo*. These results demonstrate the utility of the BAR reporter to monitor changes in AKT phosphorylation noninvasively in orthotopic human lung cancer xenograft.

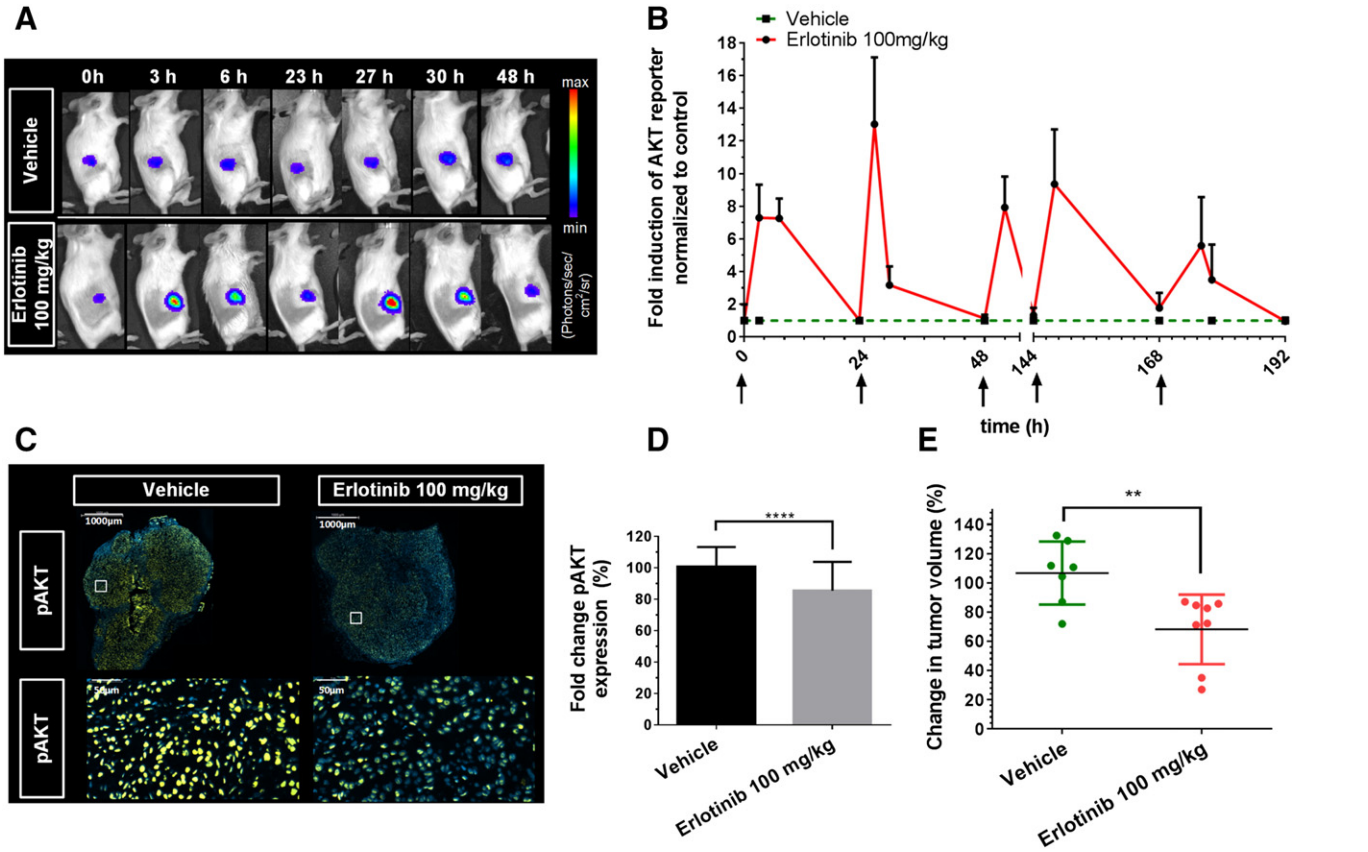

Figure 3. Erlotinib treatment results in an increase in BAR activity and a decrease in tumor growth. (A) Representative images of bioluminescence activity at indicated time points after drug administration. The signals are expressed in radiance (p/s/cm^2/sr), and the pseudocolor images were adjusted to the same threshold. (B) Time course of changes in BAR activity in control and mice treated with erlotinib at 100 mg/kg (daily for 7 days; $n = 8$). The data are presented as mean ± SEM; black arrows indicate times of drug application. (C) Representative images of IHC stained samples demonstrating diminished phosphorylation of AKT 3 hours after erlotinib treatment. Framed areas (upper pictures) are depicted as a higher magnification in the lower pictures; scale bar: 1000 μm and 50 μm. (D) The graph displays the quantification of pAKT in tumor sections. (E) Percent changes in the tumor volume at study end point (day 8); $^{**}P < .01$, $^{***} < 0.001$.

In Vivo AKT Reporter Activity Correlates with Antitumor Efficacy of Erlotinib in an Orthotopic Xenograft

We further evaluated the relationship between erlotinib-induced A549-BAR activity and antitumor efficacy in the orthotopic xenograft model. Tumor growth was monitored by µ-CT imaging. BLI signal intensities were recorded 3 hours after the treatment two times weekly, and results were correlated with the antitumoral efficacy *in vivo*. Treatment of orthotopic xenografts with 100 mg/kg erlotinib daily resulted in the highest BAR induction with up to 17-fold after the first two treatments. In comparison, the low dose (25 mg/kg) displayed a seven-fold increase in BAR activity. We observed significant signal attenuation after day 10 with erlotinib at 100 mg/kg. Here BLI signal was only eight-fold (Figure 5, *A* and *B*; $^{*}P < .05$; $^{**}.01$). Nevertheless, the BLI activity of the low and high erlotinib dose was significantly different from vehicle-treated mice at all time points and correlated with the therapeutic efficacy (Figure 5, *D* and *E*). Representative µ-CT images for each treatment group demonstrated inhibition of tumor growth (Figure 5*C*). Lung-air volume measurement once weekly by µ-CT revealed significant differences between the treatment groups (Figure 5*D*). The calculated lung-air volume was increased for 7% by erlotinib at 100 mg/kg on day 8. In contrast both, the 25-mg/kg dose and the control displayed a decrease in the lung-air volume (about 5% and 25%). Follow-up µ-CT imaging at day 12 showed a significant decrease of the lung-air volume for all groups (control, 25 and 100 mg/kg erlotinib). However, the decrease was less prominent for both of the erlotinib-treated groups, indicating diminished tumor growth (Figure 5, *C* and *D*). Concordantly to this, the lung weight from mice of the 100-mg/kg treatment group was significantly lower (Figure 5*F*). These results indicate that BAR signal translated into tumor growth reduction in orthotopic setting.

Ex Vivo Analysis of Orthotopic Xenografts Shows Unchanged pAKT and Active Caspase-3 Expression after Several Treatments with Erlotinib

The *ex vivo* analysis of pAKT, PCAN, and cleaved caspase-3 protein levels in the lungs of orthotopic A549-BAR xenografts after 12 days of erlotinib treatment (25 mg/kg and 100 mg/kg) was performed by IHC analysis.

We observed no significant differences in the pAKT staining between the treatment groups (Figure 6, *A* and *B*). Based on the results depicted in Figure 5*B*, we expected that neither 25 mg/kg nor 100 mg/kg erlotinib application reduced the AKT phosphorylation significantly after 12 days of treatment (Figure 6*A*). Regarding the PCNA protein expression, indicative of cell proliferation, there was significant reduction of 25% at the dosage of 100 mg/kg erlotinib ($P < .001$; Figure 6, *C* and *D*). The erlotinib concentration of 25 mg/kg

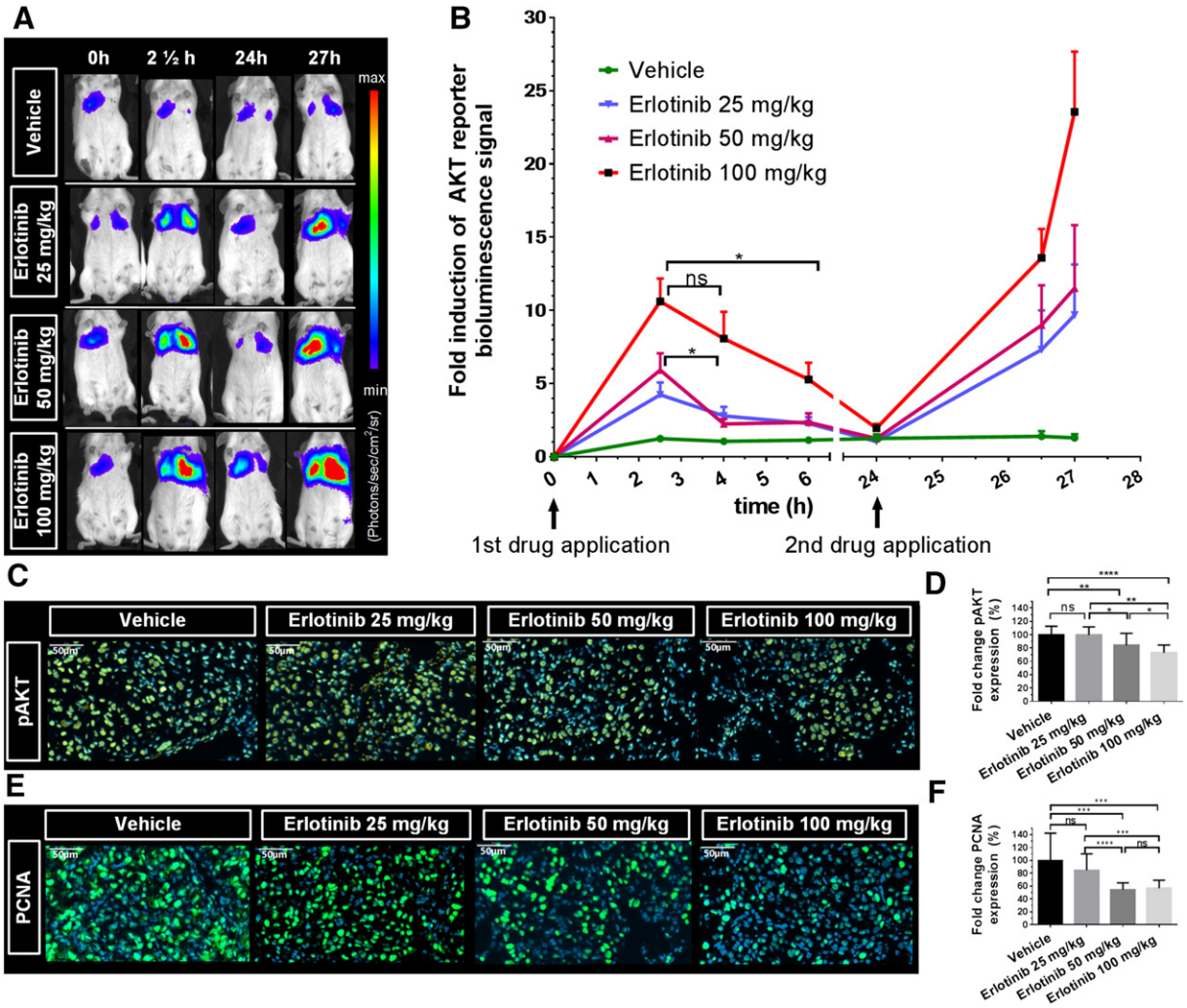

Figure 4. Molecular imaging of BAR activity *in vivo* corresponds with pAKT and cell proliferation marker (PCNA) *ex vivo.* (A) Representative BLI images visualize the pharmacodynamics of erlotinib drug treatment dependent of the dosage (25, 50, and 100 mg/kg) in A549-BAR orthotopic xenografts ($n = 4$). Signals are expressed in radiance (p/s/cm^2/sr), and the pseudocolor images were adjusted to the same threshold. (B) Time course of quantitative dynamic profile of BAR activity is displayed for each group (mean ± SEM). (C, E) IHC analysis of the lung sections for pAKT and PCNA expression. Yellow: pAKT (S473); green: PCNA; blue: cell nucleus; scale bar: 50 μm. (D, F) The graphs show the pAKT and PCNA quantification of the lung tissue sections. All fluorescence slides were scanned with the same exposure time ($t = 150$ ms) to compare images. *$P < .05$; ** < .01; *** < .001.

had no influence on the PCNA level. Additionally, we analyzed the induction of apoptosis using cleaved caspase-3. We found in both treatment groups an unchanged expression after 2 weeks of erlotinib treatment (Figure 6*E*).

Discussion

Orthotopic xenografts are of significant importance for preclinical drug research, as they offer a model organism more closely related to the clinical situation and hence have the potential for an improved prediction of responses and resistances to drugs as compared to s.c. tumor models [28–30]. The evaluation of the bioavailability and pharmacodynamic properties of AKT inhibiting compounds longitudinally within orthotopic lung cancer xenografts is needed because novel EGFR, PI3K, and AKT inhibitors are in preclinical development. The present study demonstrated the *in vitro* and *in vivo* quantification of the AKT activity (BAR imaging) in orthotopic NSCLC xenografts as well as the overall lung tumor load (µ-CT imaging) in response to erlotinib therapy. This multimodal imaging strategy provides a promising approach to monitor the phosphorylation status of AKT in an anatomical context of the lungs and thereby may facilitate the drug development of kinase inhibitors.

Using the BAR technology, it was possible to study the pharmacodynamics of erlotinib *in vitro* as well as longitudinally *in vivo*. Erlotinib inhibits selectively the tyrosine kinase domain of EGFR, which was indirectly detectable by monitoring downstream AKT activity by BAR. The time- and concentration-dependent changes of the BAR signals *in vitro* by treatment with EGFR, PI3K, or AKT inhibiting compounds correlated with the AKT dephosphorylation determined by Western blot analysis (Figure 2, *A* and *B*). In all cases, pAKT expression was closely related to the BLI signals *in vitro* (as shown by the correlation graph Figure 2*C*). Cetuximab and perifosine do not effectively increase the BAR activity and in correlation have no effect on the AKT phosphorylation (Figure 2, *A* and *B*). In concordance with other reports, cetuximab and perifosine

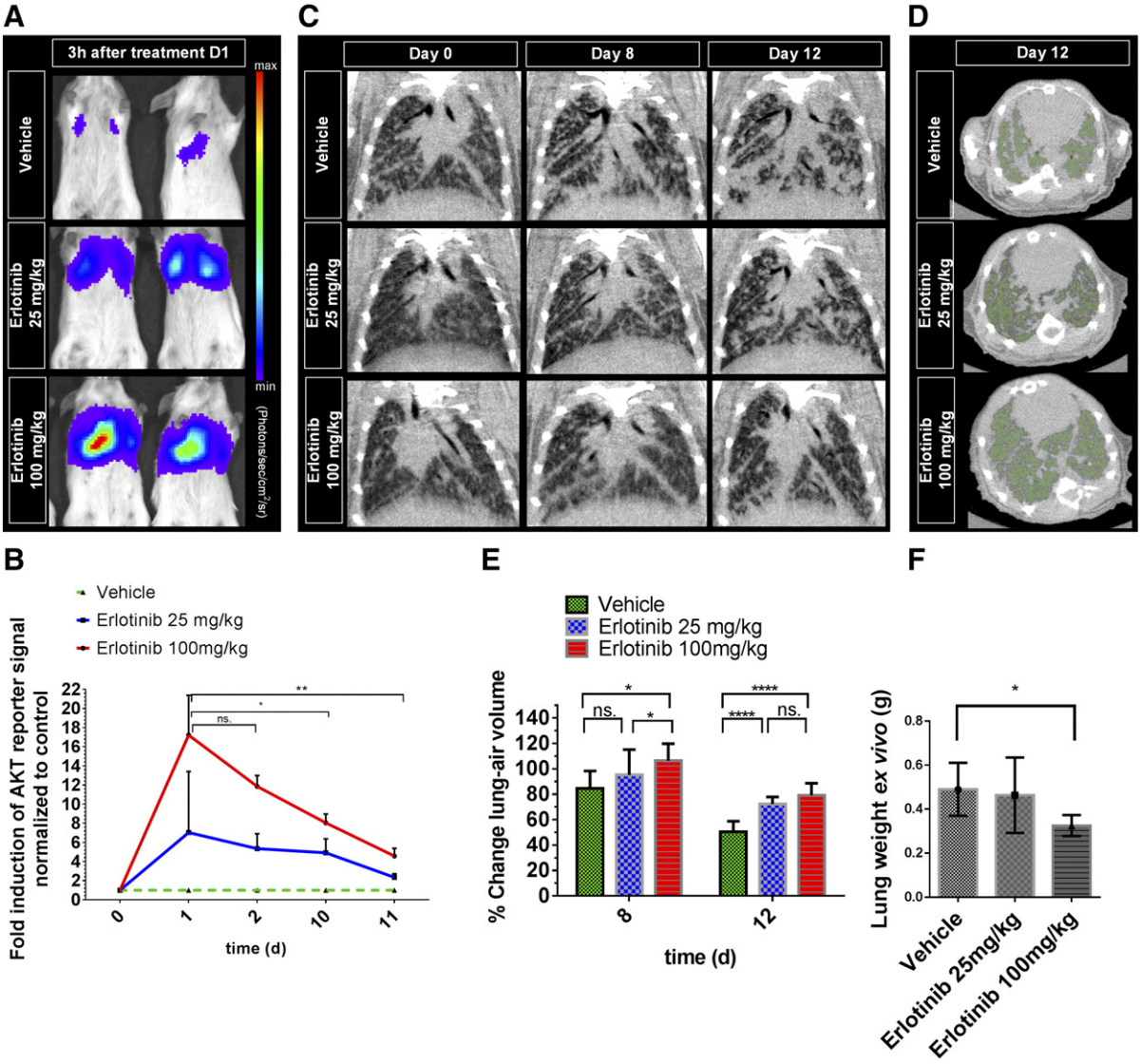

Figure 5. Micro-CT imaging detects tumor growth reduction of orthotopic A549-BAR xenografts in response to erlotinib treatment as indicated by BAR-activity. (A) Representative BLI images 3 hours after first oral application of erlotinib at various dosages. Bioluminescence signals are expressed in radiance (p/s/cm^2/sr), and the pseudocolor images were adjusted to the same threshold. (B) Pharmacodynamic time course of AKT inhibition in response to treatment with vehicle or 25 and 100 mg/kg erlotinib. Fold induction of reporter activity was normalized to the vehicle control group. (C) Representative μ-CT coronal images show the lung anatomy and tumor load before and after each treatment week. (D) Representative μ-CT axial images show the lung-air volume (green color) at d12. (E) Changes of the lung-air volumes detected by μ-CT imaging are displayed at d8 and d12. (F) Weight of explanted lungs at the study end point is shown as mean ± SD. *P < .05; ** < .01; *** < .001.

are known to be slightly effective because of the KRAS mutation and the low basal p-AKT levels in A549 the cell line [31,32]. The assay was not suitable for ATP-competitive small molecule inhibitors (like ipatasertib and AZD-5363; Figure 2, *A* and *B*), known to hyperphosphorylate AKT as a consequence of disrupted feedback regulation [33].

Regarding the *in vivo* BLI results, the inhibitory effect of different erlotinib concentrations on the BAR activity is in good agreement with the phospho-AKT levels *ex vivo* (examined by IHC analysis, Figure 4, *C* and *D*). Further, the *in vivo* BLI results were comparable with established bioavailability data of erlotinib. The maximum of the BAR signal (AKT inhibition) was monitored 2.5 to 3 hours after application of different erlotinib concentrations, which was independent of the drug concentrations (Figure 4, *A* and *B*). The BAR activity generally decreased 4 to 6 hours after treatment, indicating drug clearance or metabolism at this time point. This is in good agreements with results reporting that 100 mg/kg erlotinib is the maximal tolerable dose in mice with maximum plasma concentrations reached between 0.5 and 4 hours after delivery [34].

Regarding the imaging technologies, we chose BLI and micro-CT imaging as rapid and robust tools to study the molecular regulation of the AKT activity and correlation with the tumor burden in the lungs of free-breathing mice. Because both technologies are noninvasive, it was possible to perform longitudinally measurements over time in the same animal. Temporal quantification of intracellular kinase activity usually requires necropsy of animals at several time points. Hence, the applied noninvasive approach saves both time and animals in pharmacokinetic and pharmacodynamic studies of preclinical drug

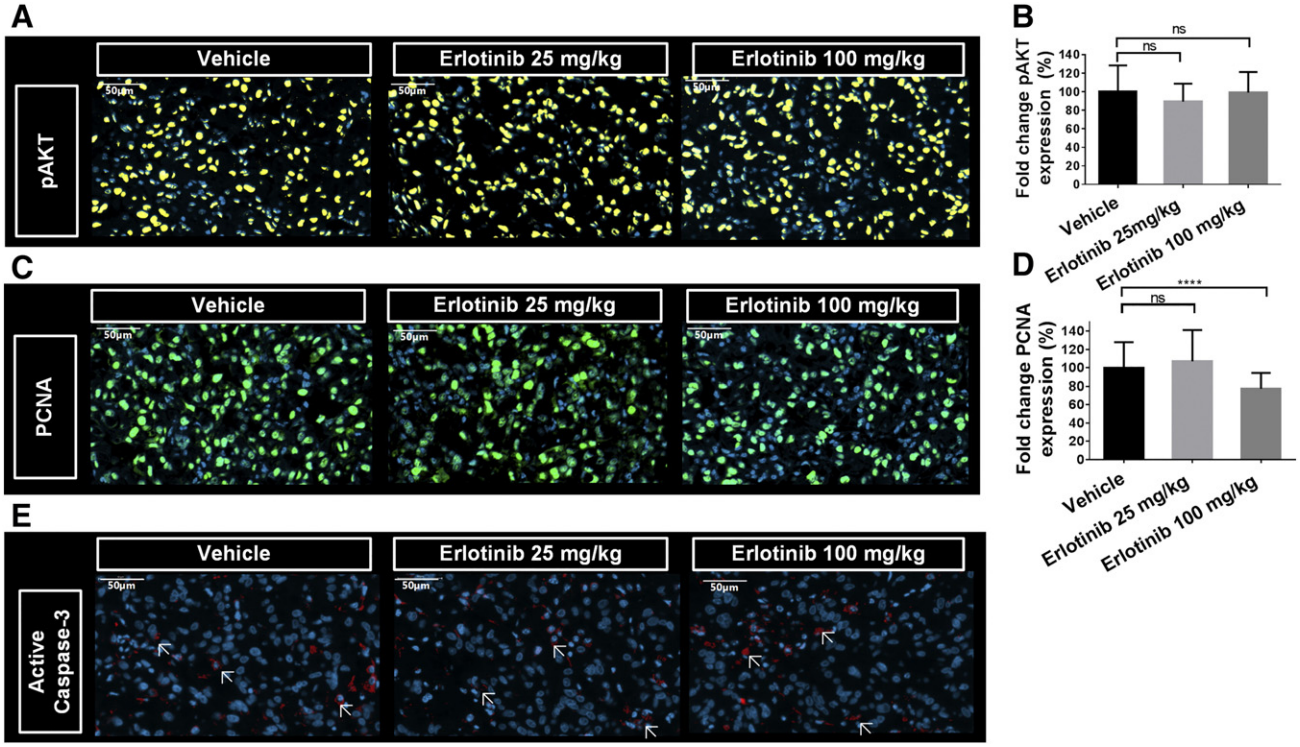

Figure 6. Modulation of pAKT, PCNA, and active caspase-3 expression after 2 weeks of erlotinib treatment. Representative histologic sections showing (A) pAKT, (C) PCNA, and (E) active caspase-3 (arrows) in control mice and after treatment with 25 mg/kg or 100 mg/kg erlotinib at the study end point (d12). The graphs display the quantification of the (B) pAKT and (D) PCNA staining. All fluorescence slides were scanned with the same exposure time (t = 150 milliseconds) to compare images. Yellow: pAKT (S473); green: PCNA; red: active caspase-3; blue: cell nucleus; scale bar, 50 μm; *** < .001.

efficacy. The tumor growth in the lungs was quantified indirectly by measuring the residual lung-air volume with micro-CT, which was described previously as a method by other studies [35,36]. This anatomical readout is needed to interpret the orthotopic BLI signals as they are dependent of the AKT inhibition and the overall tumor load. We observed a repeated BAR activation indicative for the inhibition of AKT after sequential drug application in the s.c. and orthotopic A549 xenograft models (Figures 3*B* and 4*B*). This is necessary for the therapeutic efficacy because AKT is known as a critical regulator of cancer cell survival and proliferation and high levels of phospho-AKT are linked with therapeutic resistance to TKIs [9,12]. In concordance with others, we demonstrated that erlotinib treatment slightly suppresses s.c. growing tumors [37–39]. In addition, we also observed a reduction of the orthotopic tumor volume. A relation was noticed between BLI induction and tumor growth reduction (Figures 3, *B* and *E* and 5, *B* and *E*). These results confirm that the quantification of phospho-AKT in EGFR inhibiting therapy is indicative for successful targeting and thus therapeutic efficacy *in vivo*.

After 11 days of erlotinib application in the orthotopic xenograft, the BAR signals were significantly reduced (Figure 5*B*). This correlated with the unmodulated phosphorylation of AKT at the study end point *ex vivo* (Figure 6, *A* and *B*) presumably caused by its reactivation by the induction of bypass mechanisms. The upregulation of RTK (e.g., HER family, IGF-R, c-MET, AXL), the development of secondary mutations like EGFR T790M, and aberrant downstream signaling (e.g., by PTEN loss, KRAS mutations) are described to stimulate AKT phosphorylation [40–43]. Although several *in vitro* models are described to investigate resistance mechanisms, robust *in vivo* assays are needed to obtain a more comprehensive characterization of the drug-target interaction as well as the formation of resistance.

To determine the induction of apoptosis in A549 xenograft by erlotinib treatment, we measured the caspase-3 activation *ex vivo* (Figure 6*E*). Results show that there was a lack of apoptosis induction which corresponds also with the observation from other groups [37,44]. Although apoptosis can be induced independently of caspase activation, resistance to TKIs like erlotinib may be caused by blocking apoptosis induction [45,46]. Thus, successful induction of cancer cell death can be accomplished by combination therapies, for example, with HDAC inhibitors [37]. The therapeutic advantage of AKT inhibition combined by novel proapoptotic compounds may provide a further alternative but must be proven in subsequent studies.

In conclusion, the presented study provides an approach to evaluate EGFR, PI3K, and AKT inhibitors noninvasively and to examine resistance. This technical approach provides important time- and dose-dependent pharmacodynamic insights of AKT inhibition by erlotinib *in vitro* as well as *in vivo*. We demonstrate that the BAR reporter specifically detected the therapeutic response of lung tumors to AKT inhibition. The pharmacodynamic effects of erlotinib could be monitored longitudinally in orthotopic NSCLC model. Monitoring the pharmacodynamics of EGFR pathway inhibiting small molecules by BAR imaging could be further expanded to other drug classes (e.g., siRNA, LNA, antibodies, and nanocarriers) and tumor models. Screening and analyzing of next-generation EGFR inhibitors with this approach open up perspectives for the identification of drug

candidates and combinations with efficacy to resistant cell lines. In addition, the simultaneous measurement of different readouts provides a strategy for providing more comprehensive data. Finally, this approach can be applied to optimize pharmacological intervention, drug combinations, optimization of dosages, and drug schedules in tumor xenografts.

Acknowledgements

We are indebted to Carina Hage for supporting us in the CT measurements.

References

[1] Lemjabbar-Alaoui H, Hassan OU, Yang YW, and Buchanan P (2015). Lung cancer: biology and treatment options. *Biochim Biophys Acta* **1856**, 189–210.

[2] Torre LA, Siegel RL, and Jemal A (2016). Lung cancer statistics. *Adv Exp Med Biol* **893**, 1–19.

[3] Jia Y, Yun CH, Park E, Ercan D, Manuia M, Juarez J, Xu C, Rhee K, Chen T, and Zhang H, et al (2016). Overcoming EGFR(T790M) and EGFR(C797S) resistance with mutant-selective allosteric inhibitors. *Nature* **534**, 129–132.

[4] Korpanty GJ, Graham DM, Vincent MD, and Leighl NB (2014). Biomarkers that currently affect clinical practice in lung cancer: EGFR, ALK, MET, ROS-1, and KRAS. *Front Oncol* **4**, 204.

[5] Thomas A, Liu SV, Subramaniam DS, and Giaccone G (2015). Refining the treatment of NSCLC according to histological and molecular subtypes. *Nat Rev Clin Oncol* **12**, 511–526.

[6] Stewart EL, Tan SZ, Liu G, and Tsao MS (2015). Known and putative mechanisms of resistance to EGFR targeted therapies in NSCLC patients with EGFR mutations—a review. *Transl Lung Cancer Res* **4**, 67–81.

[7] Bora-Singhal N, Perumal D, Nguyen J, and Chellappan S (2015). Gli1-mediated regulation of Sox2 facilitates self-renewal of stem-like cells and confers resistance to EGFR inhibitors in non–small cell lung cancer. *Neoplasia* **17**, 538–551.

[8] Lin L and Bivona TG (2012). Mechanisms of resistance to epidermal growth factor receptor inhibitors and novel therapeutic strategies to overcome resistance in NSCLC patients. *Chemother Res Pract* **2012**, 817297. http://dx.doi.org/10.1155/2012/817297.

[9] Janmaat ML, Kruyt FA, Rodriguez JA, and Giaccone G (2003). Response to epidermal growth factor receptor inhibitors in non–small cell lung cancer cells: limited antiproliferative effects and absence of apoptosis associated with persistent activity of extracellular signal–regulated kinase or Akt kinase pathways. *Clin Cancer Res* **9**, 2316–2326.

[10] Brognard J, Clark AS, Ni Y, and Dennis PA (2001). Akt/protein kinase B is constitutively active in non–small cell lung cancer cells and promotes cellular survival and resistance to chemotherapy and radiation. *Cancer Res* **61**, 3986–3997.

[11] Hein AL, Ouellette MM, and Yan Y (2014). Radiation-induced signaling pathways that promote cancer cell survival (review). *Int J Oncol* **45**, 1813–1819.

[12] Testa JR and Tsichlis PN (2005). AKT signaling in normal and malignant cells. *Oncogene* **24**, 7391–7393.

[13] Romashkova JA and Makarov SS (1999). NF-kappaB is a target of AKT in anti-apoptotic PDGF signalling. *Nature* **401**, 86–90.

[14] Dan HC, Ebbs A, Pasparakis M, Van Dyke T, Basseres DS, and Baldwin AS (2014). Akt-dependent activation of mTORC1 complex involves phosphorylation of mTOR (mammalian target of rapamycin) by IkappaB kinase alpha (IKKalpha). *J Biol Chem* **289**, 25227–25240.

[15] Calnan DR and Brunet A (2008). The FoxO code. *Oncogene* **27**, 2276–2288.

[16] Cantley LC (2002). The phosphoinositide 3-kinase pathway. *Science* **296**, 1655–1657.

[17] Parcellier A, Tintignac LA, Zhuravleva E, and Hemmings BA (2008). PKB and the mitochondria: AKTing on apoptosis. *Cell Signal* **20**, 21–30.

[18] Zha J, Harada H, Yang E, Jockel J, and Korsmeyer SJ (1996). Serine phosphorylation of death agonist BAD in response to survival factor results in binding to 14-3-3 not BCL-X(L). *Cell* **87**, 619–628.

[19] Hanahan D and Weinberg RA (2011). Hallmarks of cancer: the next generation. *Cell* **144**, 646–674.

[20] Altomare DA and Testa JR (2005). Perturbations of the AKT signaling pathway in human cancer. *Oncogene* **24**, 7455–7464.

[21] Fumarola C, Bonelli MA, Petronini PG, and Alfieri RR (2014). Targeting PI3K/AKT/mTOR pathway in non small cell lung cancer. *Biochem Pharmacol* **90**, 197–207.

[22] Cheng JQ, Lindsley CW, Cheng GZ, Yang H, and Nicosia SV (2005). The Akt/PKB pathway: molecular target for cancer drug discovery. *Oncogene* **24**, 7482–7492.

[23] LoPiccolo J, Blumenthal GM, Bernstein WB, and Dennis PA (2008). Targeting the PI3K/Akt/mTOR pathway: effective combinations and clinical considerations. *Drug Resist Updat* **11**, 32–50.

[24] Brindle K (2008). New approaches for imaging tumour responses to treatment. *Nat Rev Cancer* **8**, 94–107.

[25] Wang Y, Tseng JC, Sun Y, Beck AH, and Kung AL (2015). Noninvasive imaging of tumor burden and molecular pathways in mouse models of cancer. *Cold Spring Harb Protoc* **2015**, 135–144.

[26] Weber TG, Osl F, Renner A, Poschinger T, Galban S, Rehemtulla A, and Scheuer W (2014). Apoptosis imaging for monitoring DR5 antibody accumulation and pharmacodynamics in brain tumors noninvasively. *Cancer Res* **74**, 1913–1923.

[27] Zhang L, Lee KC, Bhojani MS, Khan AP, Shilman A, Holland EC, Ross BD, and Rehemtulla A (2007). Molecular imaging of Akt kinase activity. *Nat Med* **13**, 1114–1119.

[28] Bibby MC (2004). Orthotopic models of cancer for preclinical drug evaluation: advantages and disadvantages. *Eur J Cancer* **40**, 852–857.

[29] Herter-Sprie GS, Kung AL, and Wong KK (2013). New cast for a new era: preclinical cancer drug development revisited. *J Clin Invest* **123**, 3639–3645.

[30] Ruggeri BA, Camp F, and Miknyoczki S (2014). Animal models of disease: pre-clinical animal models of cancer and their applications and utility in drug discovery. *Biochem Pharmacol* **87**, 150–161.

[31] Elrod HA, Lin YD, Yue P, Wang X, Lonial S, Khuri FR, and Sun SY (2007). The alkylphospholipid perifosine induces apoptosis of human lung cancer cells requiring inhibition of Akt and activation of the extrinsic apoptotic pathway. *Mol Cancer Ther* **6**, 2029–2038.

[32] Lange F, Franz B, Maletzki C, Linnebacher M, Huhns M, and Jaster R (2014). Biological and molecular effects of small molecule kinase inhibitors on low-passage human colorectal cancer cell lines. *Biomed Res Int* **2014**, 568693. http://dx.doi.org/10.1155/2014/568693.

[33] Okuzumi T, Fiedler D, Zhang C, Gray DC, Aizenstein B, Hoffman R, and Shokat KM (2009). Inhibitor hijacking of Akt activation. *Nat Chem Biol* **5**, 484–493.

[34] Agency EM (2013). Tarceva, INN-Erlotinib. http://wwwemaeuropaeu/docs/en_GB/document_library/EPAR_-_Scientific_Discussion/human/000618/WC500033991pdf; 2013.

[35] Barck KH, Bou-Reslan H, Rastogi U, Sakhuja T, Long JE, Molina R, Lima A, Hamilton P, Junttila MR, and Johnson L, et al (2015). Quantification of tumor burden in a genetically engineered mouse model of lung cancer by micro-CT and automated analysis. *Transl Oncol* **8**, 126–135.

[36] Haines BB, Bettano KA, Chenard M, Sevilla RS, Ware C, Angagaw MH, Winkelmann CT, Tong C, Reilly JF, and Sur C, et al (2009). A quantitative volumetric micro-computed tomography method to analyze lung tumors in genetically engineered mouse models. *Neoplasia* **11**, 39–47.

[37] Chen MC, Chen CH, Wang JC, Tsai AC, Liou JP, Pan SL, and Teng CM (2013). The HDAC inhibitor, MPT0E028, enhances erlotinib-induced cell death in EGFR-TKI-resistant NSCLC cells. *Cell Death Dis* **4**, e810. http://dx.doi.org/10.1038/cddis.2013.330.

[38] Ito K, Semba T, Uenaka T, Wakabayashi T, Asada M, and Funahashi Y (2014). Enhanced anti-angiogenic effect of E7820 in combination with erlotinib in epidermal growth factor receptor-tyrosine kinase inhibitor-resistant non–small-cell lung cancer xenograft models. *Cancer Sci* **105**, 1023–1031.

[39] Naumov GN, Nilsson MB, Cascone T, Briggs A, Straume O, Akslen LA, Lifshits E, Byers LA, Xu L, and Wu HK, et al (2009). Combined vascular endothelial growth factor receptor and epidermal growth factor receptor (EGFR) blockade inhibits tumor growth in xenograft models of EGFR inhibitor resistance. *Clin Cancer Res* **15**, 3484–3494.

[40] Albury TM, Pandey V, Gitto SB, Dominguez L, Spinel LP, Talarchek J, Klein-Szanto AJ, Testa JR, and Altomare DA (2015). Constitutively active Akt1 cooperates with KRas(G12D) to accelerate in vivo pancreatic tumor onset and progression. *Neoplasia* **17**, 175–182.

[41] Huang L and Fu L (2015). Mechanisms of resistance to EGFR tyrosine kinase inhibitors. *Acta Pharm Sin B* **5**, 390–401.

[42] Lee JG and Wu R (2015). Erlotinib-cisplatin combination inhibits growth and angiogenesis through c-MYC and HIF-1alpha in EGFR-mutated lung cancer in vitro and in vivo. *Neoplasia* **17**, 190–200.

[43] Oxnard GR, Arcila ME, Chmielecki J, Ladanyi M, Miller VA, and Pao W (2011). New strategies in overcoming acquired resistance to epidermal growth factor receptor tyrosine kinase inhibitors in lung cancer. *Clin Cancer Res* **17**, 5530–5537.

[44] Hoffarth S, Zitzer A, Wiewrodt R, Hahnel PS, Beyer V, Kreft A, Biesterfeld S, and Schuler M (2008). pp32/PHAPI determines the apoptosis response of non–small-cell lung cancer. *Cell Death Differ* **15**, 161–170.

[45] Broker LE, Kruyt FA, and Giaccone G (2005). Cell death independent of caspases: a review. *Clin Cancer Res* **11**, 3155–3162.

[46] Wong MH, Xue A, Baxter RC, Pavlakis N, and Smith RC (2016). Upstream and downstream co-inhibition of mitogen-activated protein kinase and PI3K/Akt/mTOR pathways in pancreatic ductal adenocarcinoma. *Neoplasia* **18**, 425–435.